

# UC San Diego

## UC San Diego Previously Published Works

### Title

Effect of secondary convective cells on turbulence intensity profiles, flow generation, and transport

### Permalink

<https://escholarship.org/uc/item/1g58p257>

### Journal

Physics of Plasmas, 19(11)

### ISSN

1070-664X

### Authors

Yi, S  
Kwon, JM  
Diamond, PH  
[et al.](#)

### Publication Date

2012-11-01

### DOI

10.1063/1.4767652

### Copyright Information

This work is made available under the terms of a Creative Commons Attribution-NonCommercial-NoDerivatives License, available at <https://creativecommons.org/licenses/by-nc-nd/4.0/>

Peer reviewed

# Effect of secondary convective cells on turbulence intensity profiles, flow generation, and transport

S. Yi,<sup>1</sup> J. M. Kwon,<sup>1</sup> P. H. Diamond,<sup>1,2</sup> and T. Rhee<sup>1</sup>

<sup>1</sup>National Fusion Research Institute, Eoeun-dong, Yuseong-gu, Daejeon 305-333, South Korea

<sup>2</sup>Center for Astrophysics and Space Sciences and Department of Physics, University of California San Diego, La Jolla, California 92093-0429, USA

(Received 18 July 2012; accepted 1 November 2012; published online 28 November 2012)

This paper reports the results of gyrokinetic simulation studies of ion temperature gradient driven turbulence which investigate the role of non-resonant modes in turbulence spreading, turbulence regulation, and self-generated plasma rotation. Non-resonant modes, which are those without a rational surface within the simulation domain, are identified as nonlinearly driven, radially extended convective cells. Even though the amplitudes of such convective cells are much smaller than that of the resonant, localized turbulence eddies, we find from bicoherence analysis that the mode-mode interactions in the presence of such convective cells increase the efficiency of turbulence spreading associated with nonlocality phenomena. Artificial suppression of the convective cells shows that turbulence spreading is reduced, and that the turbulence intensity profile is more localized. The more localized turbulence intensity profile produces stronger Reynolds stress and  $E \times B$  shear flows, which in turn results in more effective turbulence self-regulation. This suggests that models without non-resonant modes may significantly underestimate turbulent fluctuation levels and transport. © 2012 American Institute of Physics. [<http://dx.doi.org/10.1063/1.4767652>]

## I. INTRODUCTION

We know that self-generated sheared plasma flows play a crucial role in reducing turbulence and anomalous transport. The combined system of plasma turbulence and flow regulates and organizes itself. In the presence of a shear flow, turbulence eddies are stretched, so that perpendicular wave number increases. As a result of this, the growth rate and the autocorrelation time of turbulent fluctuations decrease, leading to suppression of turbulence.<sup>1,2</sup> The poloidal zonal flow is generated by nonlinear processes—such as modulational instability—in the fluctuation spectrum or the divergence of the radial flux of wave momentum or Reynolds stress.<sup>1,3,4</sup> Thus, the saturation and self-organization process of turbulence and zonal flows are affected by the fluctuation intensity profile. On the other hand, the spatial spreading of turbulence, which can alter the turbulence intensity profile, is coupled to the spectral transfer of fluctuation energy through nonlinear mode-mode interactions in an inhomogeneous system.<sup>5–10</sup> Thus, we expect that modification of spectral transfer will alter the dynamics of flows and the subsequent fluctuation profile structure and transport. By experimenting with switching on/off various classes of nonlinear interactions, we can elucidate the relation between those nonlinear interactions, turbulence spreading, the intensity profile, and the self-generation of zonal flow.

There are interesting results of numerical simulations which link the spectral transfer of fluctuation energy to the self-organization process. From previous gyrofluid and gyrokinetic simulations, qualitatively different transport phenomena were observed in studies with different populations of non-resonant modes (i.e., modes without a rational surface where  $q(r) = m/n$  within the simulation domain) in the fluctuation spectra.<sup>11–14</sup> Here  $m$ ,  $n$ , and  $q(r)$  denote the poloidal

and toroidal mode numbers of fluctuating potentials, and the safety factor, respectively. Since non-resonant modes, which have a finite parallel wave number  $k_{\parallel} \sim m - nq \neq 0$ , are usually stable in linear theory, they are readily distinguished from linearly excited, localized turbulence eddies, which correspond to linearly unstable resonant modes.

The non-resonant modes are related to the poloidally (and toroidally) localized envelope of fluctuations, which is composed of a large number of poloidal and toroidal modes. These fluctuation envelopes have radially extended structure with non-vanishing  $k_{\parallel}$ . Even though the envelopes are radially extended and have streamer-like structure, they can and should be distinguished from the streamer structure generated by superposition of linearly unstable resonant modes.<sup>15</sup> Interestingly, the radially extended envelopes evolve through nonlinear processes such as mode-mode interactions, so they may be considered as secondary convective cells. The radially extended convective cells can be associated with streamers observed in flux-driven turbulence simulations,<sup>16,17</sup> which are excited intermittently by nonlinear mode-mode interaction processes.<sup>18–21</sup> The amplitude and dynamics of the convective cells depend on aspects of the simulation models, such as the representation of turbulence spectrum and method of turbulence drive—how non-resonant modes are incorporated and whether the free energy source is constant or decays in time, for example. Note that these convective cells differ from the traditional picture, in which the cells are flute-like ( $k_{\parallel} = 0$ ) and quasi-coherent.<sup>22,23</sup>

The radially extended convective cells can modify the spatial profile and propagation of turbulence through the process of turbulence spreading. We can relate mode-mode interactions among only resonant modes in spectral space to the spatial spreading of fluctuation by using the fact that a ( $m$ ,  $n$ ) resonant mode is localized around its rational surface

with a finite, usually limited, radial extent. Nonlinear interactions between overlapping resonant modes, which are situated on different but nearby flux surfaces, can transfer energy not only in spectral space but also in position space. This results in spectral energy transfer in radius—so called turbulence spreading. Turbulence spreading is often thought of as a diffusive process because the radial flux of turbulence energy caused by numerous mode-mode interactions can be modeled by a random walk with a short step size. A simple equation of turbulence spreading has been derived from a Fokker-Planck-type analysis of the evolution of turbulence intensity.<sup>8</sup> Now, let us consider mode-mode interactions in the presence of the radially extended convective cells. The interactions including the non-resonant modes—i.e., the convective cells—can effectively spread fluctuation energy to more distant radii in a single, large step, thus driving a broad fluctuation intensity profile. In Fig. 1, we contrast the mode-mode interactions (a) among resonant modes only and (b) including non-resonant modes. Based on this consideration, we can suggest that the radially extended convective cells significantly affect the couplings among the resonant modes and therefore the turbulence intensity profile. We expect that, by artificially suppressing the convective cells, longer range interactions will be limited, and so turbulence spreading should decrease. With non-resonant modes, turbulence spreading becomes a nonlocal process.

Reduced turbulence spreading by suppression of radially extended convective cells affects the self-regulation dynamics of turbulence and flows by changing the intensity profile and pattern of radial propagation of turbulence. The weaker spreading localizes the turbulence intensity profile more sharply. In turn, the turbulence intensity profile is closely related to the Reynolds stress component responsible for zonal flow generation by the familiar equation<sup>3</sup>

$$\frac{\partial \langle V_{E \times B} \rangle}{\partial t} = -\frac{\partial \langle v_r v_\theta \rangle}{\partial r} = v_{T0}^2 \rho_0^2 \frac{\partial}{\partial r} \sum_{\mathbf{k}} k_r k_\theta \phi_{\mathbf{k}}^2 \sim -\frac{\partial \langle \phi^2(r) \rangle}{\partial r}. \tag{1}$$

Therefore, a more peaked turbulence intensity profiles result in stronger zonal flow shear. Conversely, the radially extended convective cells can enhance the level of turbulence by reducing the generation of zonal flow and so weakening the self-regulation process. This impacts overall transport and self-regulation phenomena, such as intrinsic plasma flows driven by turbulence, etc. The overall process is summarized in Fig. 2.

In this paper, we present results of gyrokinetic simulations which elucidate the role of nonlinear mode-mode interactions and turbulence spreading on the self-regulation dynamics of plasma turbulence and flows, with special focus on the role of non-resonant modes. Analyzing the non-resonant mode spectrum, we show that the non-resonant modes are nonlinearly driven cells with larger  $k_{\parallel}$  and broader radial extent, as compared to the resonant modes. The latter correspond to the familiar case of radially localized turbulence eddies. From this observation, we identify the non-resonant modes as radially extended, secondary convective cells. To demonstrate the effects of radially extended convective cells on turbulence profile evolution and zonal flow generation, we can artificially control and vary the allowed values of  $k_{\parallel}$  for the fluctuating potential in the simulation. Using a bicoherence analysis, we find that by restricting the allowed values of  $k_{\parallel}$  and thereby suppressing the radially elongated convective cells, local interactions among the resonant modes are enhanced and energy transfer between radially distant modes becomes weaker. This implies that the range of scattering of fluctuation energy in spectral and configuration space simultaneously decreases. As a consequence, the profile of turbulence intensity is more localized in radial position and so zonal flows are stronger and turbulence fluctuation levels are lower. We argue that this result demonstrates that non-resonant cells are important to the dynamics of turbulence saturation by their effect on intensity profiles via increased turbulence spreading.

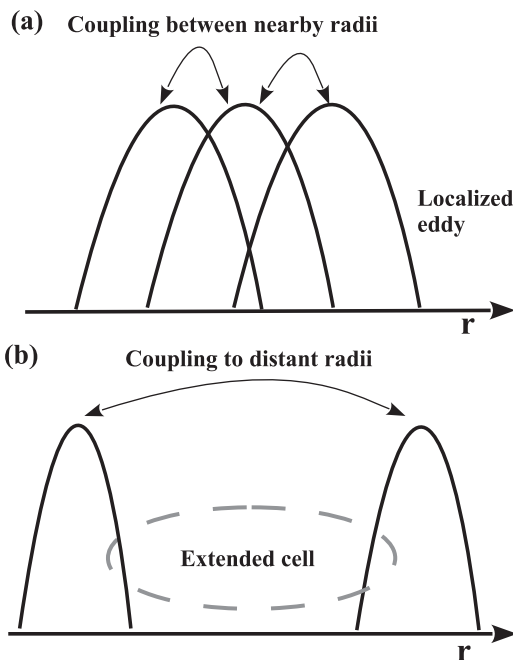


FIG. 1. Cartoon of the spatial extent of mode-mode interactions (a) among resonant modes only and (b) involving non-resonant modes.

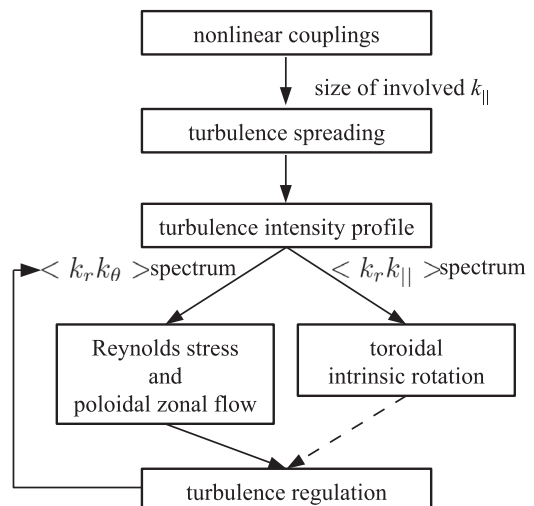


FIG. 2. Role of turbulence spreading in flow generation and transport.

The organization of the remainder of this paper is as follows: In Sec. II, we present our gyrokinetic simulation model, the method to control the excitation of non-resonant modes, and the details of the spectral analysis of turbulence, including the bicoherence analysis. In Sec. III, we compare non-resonant modes to resonant modes and identify them as radially extended, secondary convective cells. Then, we demonstrate the connection between nonlinear interactions and turbulence spreading by varying the degree of excitation of the convective cells. In Sec. IV, we compute the turbulence-driven Reynolds stress and discuss the relation between the turbulence intensity profile and generation of Reynolds stress. Effects on the turbulence regulation and transport are presented in Sec. V. In Sec. VI, we briefly report effects of turbulence spreading on toroidal rotation. Finally, the conclusions are given in Sec. VII.

## II. SIMULATION MODEL AND ANALYSIS METHOD

### A. Global gyrokinetic particle in cell code

In this study, we use a global  $\delta f$  gyrokinetic particle in cell code gKPSP.<sup>24</sup> gKPSP solves the electrostatic gyrokinetic equation.<sup>25</sup> The fluctuating potential,  $\delta\Phi$ , which obeys the gyrokinetic Poisson equation,<sup>25</sup> is represented using the following quasi-ballooning representation for efficient modeling of turbulent eddies aligned along equilibrium magnetic field lines<sup>26,27</sup>

$$\delta\Phi(t, \mathbf{x}) = \sum_{i,j,n} \Phi_{ijn}(t) Q_i(\psi) Q_j(\theta) \exp\{-in[\varphi - S_i(\theta)]\}. \quad (2)$$

Here  $\psi$  and  $\theta$  are the radial and poloidal variables, with spatial index  $i$  and  $j$ , respectively. For the toroidal variable  $\varphi$ , a spectral representation is adopted with toroidal mode number  $n$ .  $Q_i(\psi)$  and  $Q_j(\theta)$  denote quadratic spline functions centered at  $\psi_i$  and  $\theta_j$ . The numbers of radial and poloidal grid points for these spline functions are  $N_\psi$  and  $N_\theta$ , respectively.  $S_i(\theta)$  is a phase factor at a flux surface  $\psi = \psi_i$  and given by

$$S_i(\theta) = \int_0^\theta d\theta' \left. \frac{\mathbf{B} \cdot \nabla \varphi}{\mathbf{B} \cdot \nabla \theta'} \right|_{\psi_i}.$$

Figure 3 illustrates spectrum of the fluctuating potential represented by Eq. (2) and represents the resonant and non-resonant modes. Non-resonant modes are not localized “near” a flux surface. More details and verification of the simulation model are presented in Ref. 24.

The evolution of the fluctuation intensity envelope is affected by the population of non-resonant modes. To control the population of non-resonant modes allowed in the simulation, we change the number of grid points for  $Q_j$  in Eq. (2), i.e., we vary  $N_\theta$ . We set  $N_\theta = 32$  for a proper representation of the fluctuating potential with a full population of non-resonant modes. To suppress the envelope evolution artificially, we reduce the number to  $N_\theta = 6$ . Note that the number of  $N_\theta = 6$  is the minimum possible in our numerical scheme. Even though we set  $N_\theta = 6$ , a few non-resonant modes

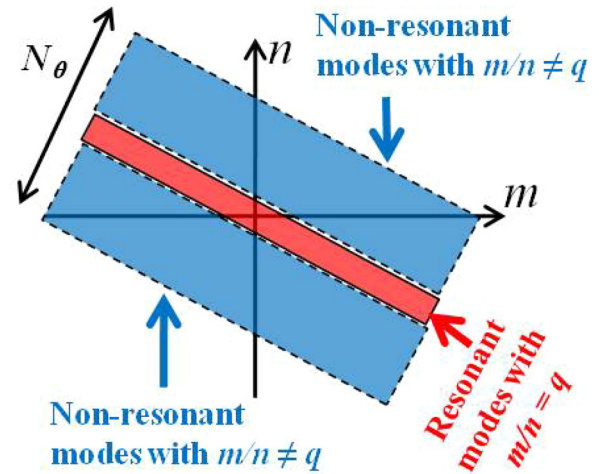


FIG. 3. Illustration of resonant and non-resonant modes on a flux surface.

remain within the simulation domain. In what follows, we refer, respectively, the  $N_\theta = 32$  and  $N_\theta = 6$  cases as “with” and “without” the non-resonant modes, for convenience.

*It should be noted that there is no profile control during the simulations. Turbulence is excited by temperature gradient and produces heat transport until free energy in the temperature gradient is exhausted. Therefore, temperature profiles relax in time and the turbulence eventually decays. Due to this limit, the excitations of the secondary convective cells are limited and their nonlinear evolution cannot be fully addressed in this work. However, we do observe clear impact of non-resonant modes and associated convective cells on the turbulence evolution, in general, and on the intensity profile, in particular.*

Simulation parameters and profiles are set as follows: A concentric circular equilibrium is used with major radius  $R_0 = 130$  cm and minor radius  $a = 48$  cm. We consider a  $q$ -profile with normal shear. Safety factor and magnetic shear at the mid-minor radius  $r = 0.5a$  are  $q = 1.43$  and  $\hat{s} = 0.78$ . The  $q$  values at the innermost and outermost surfaces are  $q_0 = 0.85$  and  $q_a = 3.02$ , respectively. Electrostatic ion temperature gradient (ITG) driven turbulence is excited by an initial temperature profile with radial gradient  $R_0/L_{Ti} = 7.14$ , and the radial gradient of the density profile  $R_0/L_{ne}$  is set to satisfy  $\eta_i = L_{ne}/L_{Ti} = 3.1$  at  $r = 0.5a$ . Velocities are normalized by  $v_{T0} = \sqrt{T_0/m_i} = 4.90 \times 10^7$  cm/s and time by  $\tau_s = R_0/v_{T0} = 2.65 \mu\text{s}$ , where  $v_{T0}$  and  $T_0 = 5$  keV are the ion thermal velocity and ion temperature in the center of a deuterium plasma, respectively. The normalized value of the ion Larmor radius on axis is  $\rho_{i0}/a = 0.011$ . The fluctuating potential is the usual dimensionless quantity  $\phi = e\delta\Phi/T_0$ . The number of radial grid points in Eq. (2) is set as  $N_\psi = 192$ . The range of toroidal mode number is chosen as  $[-32, 32]$ , for which  $|k_\theta \rho_i| \leq 0.9$  at  $r = 0.5a$ . We use a medium number of 40 M markers (100 markers per a grid) to demonstrate physics related to the convective cells. We additionally perform a convergence study to confirm the physical non-resonant mode amplitude and related issues by increasing the number of marker particles by 4 times.

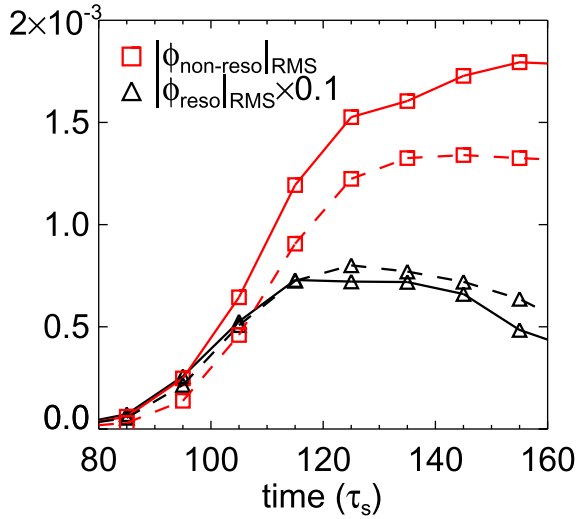


FIG. 4. Time histories of volume integrated, root-mean-square amplitude of non-resonant and resonant modes for simulations with 40 M markers (solid) and 160 M markers (broken).

### B. Convergence study and numerical property of parallel filter

Numerical noise in particle in cell simulations often contaminates important physical results. In this subsection, we present the convergence of key properties of non-resonant modes with varying marker numbers. In Fig. 4, the root-mean-square amplitudes of resonant and non-resonant modes  $\sqrt{\langle \phi^2 \rangle}$  are plotted for simulations with 40 M and 160 M marker particles. Here,  $\langle \phi^2 \rangle$  is defined as

$$\langle \phi^2 \rangle \equiv \frac{1}{V} \int dV \sum_{m,n \in \mathcal{K}} \phi_{m,n}^2(r),$$

where  $\mathcal{K}$  is a set of  $(m, n)$  defined as  $\mathcal{K} = \{(m, n) | q_{\min} \leq m/n \leq q_{\max}\}$  for the resonant modes,  $\mathcal{K} = \{(m, n) | m/n < q_{\min} \text{ or } q_{\max} < m/n\}$  for the non-resonant modes, and  $V$  is the volume of the simulation domain. While the number of marker particles increases by 4 times, the root-mean-square amplitude of the non-resonant modes decreases by only about 20%. We also show the local poloidal spectra of potential fluctuations of toroidal mode  $n = -6$  at  $r/a \approx 0.4$  for the

different numbers of markers in Fig. 5(a). From the similar levels of non-resonant components of the simulations with 40 M and 160 M markers, we can see that even the low-amplitude, physical non-resonant modes are well-resolved. The non-resonant modes are artificially filtered out by decreasing the number of poloidal grids, as shown in Fig. 5(b). In the simulations with the larger marker particles, the bicoherence analysis and profiles of turbulence intensity, Reynolds stress, and zonal flow also show the same trend with those in the simulations with the medium number of marker particles. (More detailed comparisons are presented in the forthcoming sections.) This convergence of the results in number of marker particles demonstrates that the properties of non-resonant modes and their effects are physical results.

We note that the numerical method employed in this study to suppress non-resonant modes is basically equivalent to the field-aligned Fourier filter in Ref. 28. In the previous study,<sup>28</sup> it was noted that too narrow  $k_{\parallel}$  filtering of fluctuating potential can lead to incorrect linear dynamics of ITG turbulence. To check the linear response of ITG turbulence with the different  $N_{\theta}$  values used in this work, we perform linear ITG simulations with  $N_{\theta} = 6$  and 32. In Fig. 6, the time evolutions of fluctuating potentials and linear growth rates are plotted. The results of  $N_{\theta} = 6$  and 32 show good agreement, which confirms that the numerical method used in this study preserves the linear dynamics of ITG turbulence very well and only controls non-resonant mode population in nonlinear phase.

### C. Spectral analysis of turbulence

Comprehensive spectral analyses are performed in 3-dimensional configuration space  $(r, \theta, \varphi)$  and also in time (if necessary), so as to distinguish the propagation direction of the modes. The spectral component of fluctuating potential is expressed in the Fourier form as

$$\phi(\mathbf{x}, t) = \sum_{k_r, m, n, \omega} \phi_{k_r, m, n, \omega} \exp[i(k_r r + m\theta - n\varphi - \omega t)]. \quad (3)$$

We also measure bicoherence among poloidal and toroidal modes,  $\phi_{m,n}$ , in order to quantitatively compare the

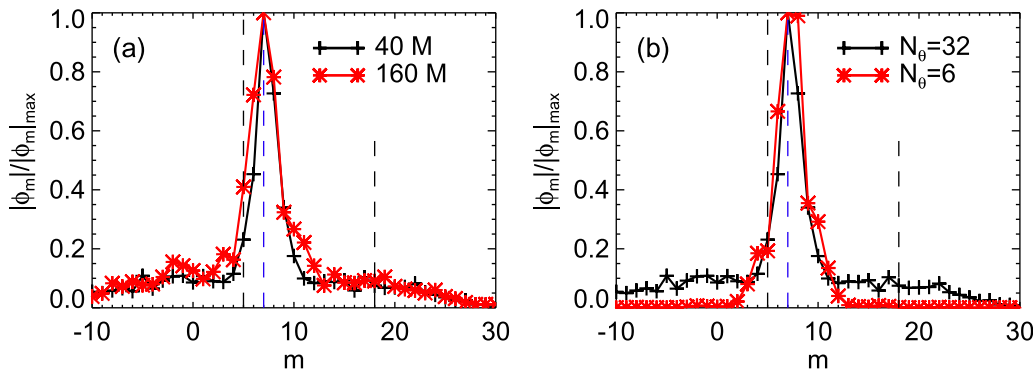


FIG. 5. Local poloidal spectra of potential fluctuations of toroidal mode  $n = -6$  at  $r/a \approx 0.4$  (a) for different marker numbers of 40 M (black) and 160 M (red) with  $N_{\theta} = 32$  and, (b) for different poloidal grid numbers of  $N_{\theta} = 6$  and 32 with 40 M markers. The spectra are averaged over the period  $t = 100 - 110\tau_s$ . The blue and black vertical lines show the local resonant mode (i.e.,  $nq(r)$ ) and the range of possible resonant mode within the simulation domain (i.e.,  $m_{\min(\max)} = nq_{\min(\max)}$ ), respectively.

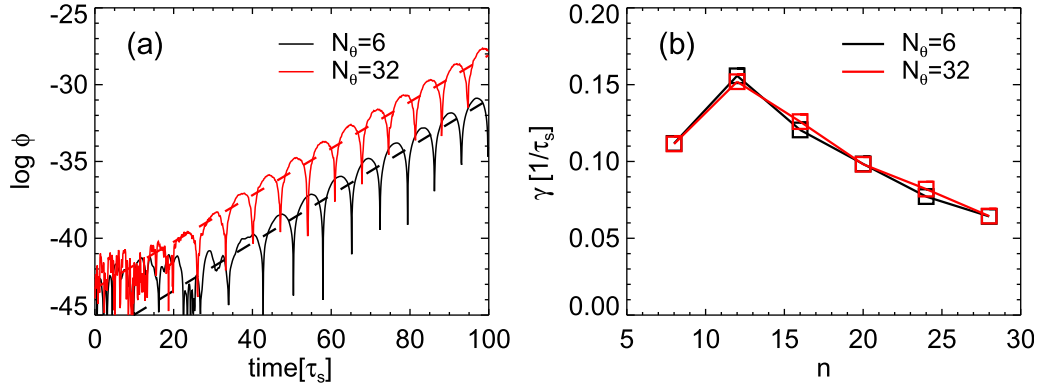


FIG. 6. (a) Time histories of  $n = 12$  mode amplitudes at  $r/a = 0.5$  and (b) linear growth rate spectra of linear simulations with  $N_\theta = 6$  and  $N_\theta = 32$ .

strength of nonlinear interactions. Specifically, we refer to quadratic interactions of  $(m_1, n_1) + (m_2, n_2) \leftrightarrow (m_1 + m_2, n_1 + n_2)$ , which need not to be radially local. Bispectral analysis is a well-established method to evaluate the relative strength of quadratic interactions.<sup>29,30</sup> The bispectrum can be written in terms of the Fourier components as

$$B_{n_1, n_2, m_1, m_2}(r_1, r_2, r_3) = \langle \phi_{m_1, n_1}(r_1) \phi_{m_2, n_2}(r_2) \phi_{m_1+m_2, n_1+n_2}^*(r_3) \rangle, \quad (4)$$

where the angle bracket indicates an average over realizations. By adopting the ergodic hypothesis, this is replaced by average over a time period about  $20\tau_s$ , which is about the time scale of evolution of the turbulence intensity profile. The bicoherence is defined in terms of the bispectrum with the normalization

$$b_{n_1, n_2, m_1, m_2}^2(r_1, r_2, r_3) = \frac{|B_{n_1, n_2, m_1, m_2}(r_1, r_2, r_3)|^2}{\langle |\phi_{m_1, n_1}(r_1) \phi_{m_2, n_2}(r_2)|^2 \rangle \langle |\phi_{m_1+m_2, n_1+n_2}(r_3)|^2 \rangle}. \quad (5)$$

The bicoherence is bounded by  $0 \leq b^2 \leq 1$  and will have a finite, non-zero value for mode numbers among which a nonlinear interaction has taken place. Larger bicoherence indicates stronger interaction.

### III. NONLINEAR INTERACTIONS AND TURBULENCE SPREADING

To compare the structure of non-resonant modes to that of resonant modes, we estimate the effective mean square parallel wave number  $\langle k_{\parallel, \text{eff}}^2 \rangle$  and the radial extent  $\langle (\Delta r)^2 \rangle$  of both resonant and non-resonant modes. These quantities are defined as

$$\langle k_{\parallel, \text{eff}}^2 \rangle \equiv \frac{1}{N} \sum_{m, n \in \mathcal{K}} \frac{\int dr [(m/q(r) - n)/R_0]^2 \phi_{m, n}^2(r)}{\int dr \phi_{m, n}^2(r)},$$

$$\langle (\Delta r)^2 \rangle \equiv \frac{1}{N} \sum_{m, n \in \mathcal{K}} \frac{\int dr (r - r_0)^2 \phi_{m, n}^2(r)}{\int dr \phi_{m, n}^2(r)},$$

respectively. Here,  $N$  and  $r_0$  are the total number of the entries and the center of each envelope, respectively. Time

histories of the above quantities are shown in Fig. 7. The onset of the nonlinear phase of turbulence occurs around  $t \approx 110\tau_s$ . The effective parallel wave number of the non-resonant modes is larger than that of the resonant modes, so the non-resonant modes experience stronger Landau damping. In spite of this stabilizing effect, the amplitude of the non-resonant modes grows continuously during the nonlinear phase, as shown in Fig. 4. This implies that the non-resonant modes are nonlinearly driven. The non-resonant modes have broader radial extent than the resonant modes, as shown in Fig. 7(b). The radial extent of the resonant modes is mainly determined by the linear theory of low- $k_{\parallel}$  ballooning mode structure during the linear phase. We note that in the nonlinear phase, the radial extent of the resonant modes

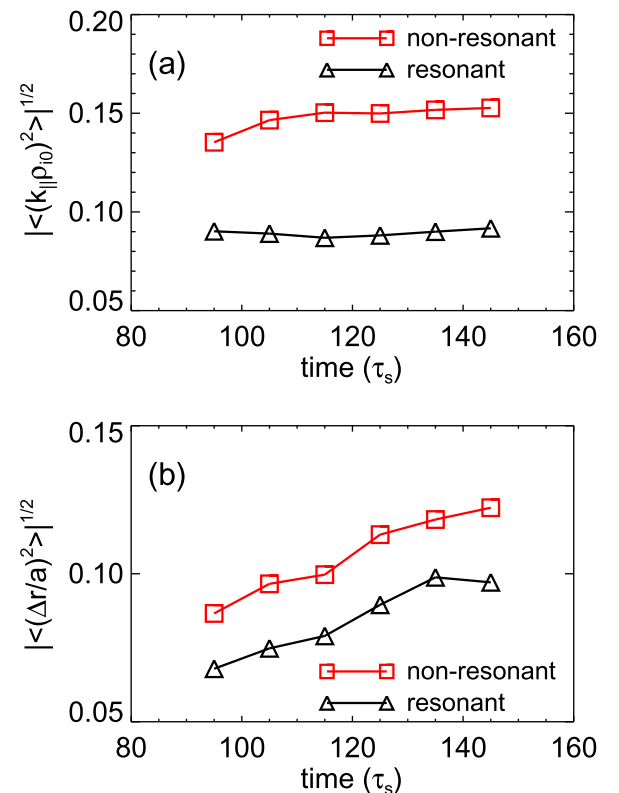


FIG. 7. Time histories of (a) effective mean square parallel wave number and (b) mean square radial extent of resonant and non-resonant modes for simulations with 40 M markers.

continuously increases, instead of remaining unchanged. The evolution of  $\langle(\Delta r)^2\rangle$  of the resonant modes cannot be understood by the linear ballooning mode theory and requires a theory incorporating nonlinear mode-mode couplings, spectral spreading, or other nonlinear effects. We do not have a clear explanation for this radial extent evolution, which is beyond the scope of this work.

We also estimate spatial correlation of resonant and non-resonant modes. Many, but not all, non-resonant modes have a coherent radial structure. As an example, we show radial structure and  $k_r$  power spectrum of a non-resonant mode with  $m/n = 1/-7$ , averaged over the period  $t = 130 - 140\tau_s$ , in Fig. 8. The correlation length can be estimated as  $\delta_c \approx 4/\Delta k \sim 0.16a \sim 14\rho_{i0}$  from the width of the dominant peak in the spectrum. This value is larger than the correlation length of resonant modes  $\delta_c \sim 5 - 7\rho_{i0}$ .

Based on these observations, the spectrum of the non-resonant modes can be associated with nonlinearly driven, radially extended structures, as compared to the resonant modes, which correspond to localized eddies that evolve from linear instability. Thus, we identify the non-resonant modes as a type of radially extended, secondary convective cell. These cells differ from the traditional concept of “convective cell,” though, in that they have finite  $k_{\parallel}$  and a finite life time, as opposed to being flute-like and quasi-coherent.<sup>22,23</sup> The radially extended convective cells have a structure similar to that of streamers. However, the large  $k_{\parallel}$

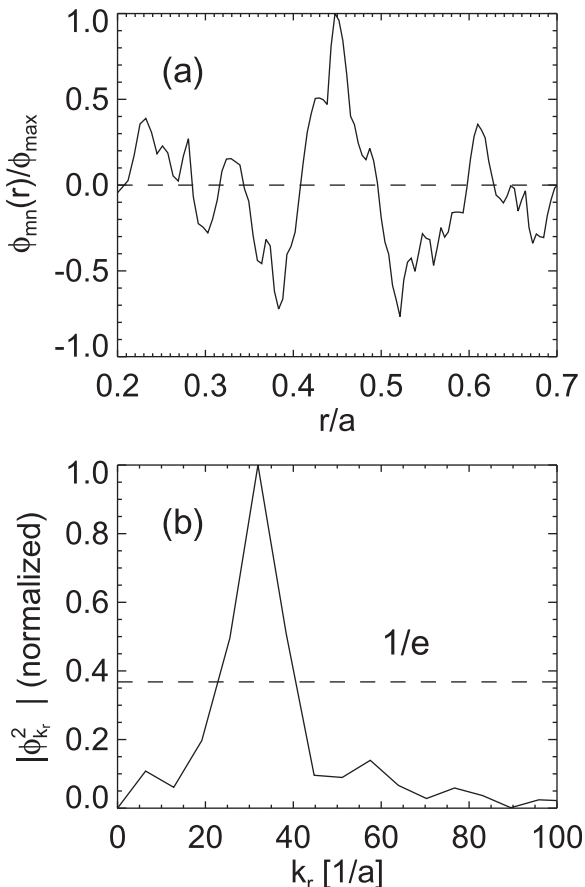


FIG. 8. (a) Radial structure and (b)  $k_r$  power spectrum of a non-resonant mode with  $m/n = 1/-7$  for simulations with 40 M markers.

of the convective cell distinguishes them from the well-known linear streamer.<sup>15</sup> On the other hand, the convective cells may be related to nonlinearly driven streamers observed in simulations.<sup>16-18</sup> Furthermore, we can expect that turbulence spreading efficiency increases with nonlinear interactions including the non-resonant modes associated with radially extended cells.

We measure changes in nonlinear interactions according to the degree of control of the radially extended convective cells by calculating the bicoherence in Eq. (5). First, we examine local mode-mode interactions which take place on a given flux surface, that is  $r_1 = r_2 = r_3 = r$ , by computing the “local” bicoherence. Figure 9 shows the local bicoherences (a) with, and (b) without, the non-resonant modes in an early ( $t = 100 - 120\tau_s$ ) and later ( $t = 120 - 140\tau_s$ ) phase of the nonlinear evolution. Data are taken from  $r/a = 0.54$  and the toroidal mode for this figure is chosen as  $n_1 = n_2 = -5$ . The results for other toroidal modes show a similar trend.

In each plot, the black, broken lines denote the resonant poloidal mode number at the radial position and; the red, broken lines show the range of possible resonant poloidal mode numbers within the simulation domain, i.e.,  $m_{\min(\max)} = nq_{\min(\max)}$ . Thus, the interior of the triangle made by the two red broken lines and the  $m_1 = m_2$  line corresponds to the interactions among the resonant modes having their own rational surfaces within the simulation domain. The region outside of the triangle corresponds to interactions involving the non-resonant modes, which arise from radially extended convective cells, which can couple to fluctuations at distant radii.

For the two cases of retaining and suppressing the convective cells, the local interactions among resonant modes are dominant in the early stage of the nonlinear phase. Differences in evolution emerge in the later nonlinear phase. The local interactions among the resonant modes decrease for the case which retains convective cells, as shown in Fig. 9(a). On the other hand, when we suppress the convective cells in Fig. 9(b), the local resonant mode interactions remain strong, even in the later nonlinear phase. We expect that the stronger local interactions result in decrease in the spectral scattering of fluctuation energy away from the local region of excitation, and so cause a more peaked turbulence intensity profile. In other words, the degradation of the local interactions upon inclusion of non-resonant convective cells indicates that such non-resonant modes mediate longer range interactions.

The expected effect of the local resonant mode interactions on turbulence spreading is shown by the time evolution of turbulence profiles in Fig. 10. By suppressing the convective cells, the turbulence profile forms a more localized peak at  $t \approx 130\tau_s$  due to the stronger local interactions among the resonant modes. In addition to this observation, we quantitatively evaluate nonlocal interactions which occur between modes at different radii by computing average bicoherence over the total interactions, defined as

$$\bar{b}^2(r, r + \delta r) \equiv \frac{1}{N_{inter}} \sum_{n_1, n_2, m_1, m_2} b_{n_1, n_2, m_1, m_2}^2(r, r, r + \delta r),$$

where  $b_{n_1, n_2, m_1, m_2}^2$  is given by Eq. (5). Here, we restrict  $r_1 = r_2 = r$  for simplicity and  $N_{inter}$  is the total number of interactions.

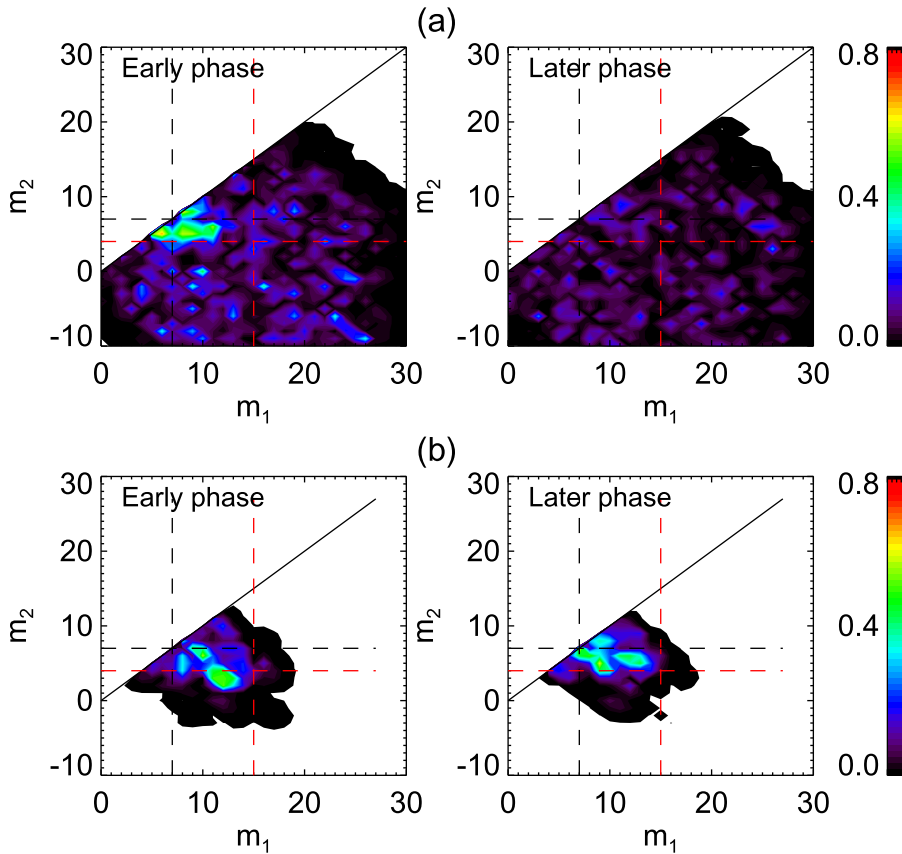


FIG. 9. Local bicoherences of the potential fluctuations (a) with, and (b) without, non-resonant modes in an early ( $t = 100 - 120\tau_s$ ) and later ( $t = 120 - 140\tau_s$ ) phase of the nonlinear evolution for simulations with 40 M markers. Interactions among three modes such that  $(m_1, n_1) + (m_2, n_2) \leftrightarrow (m_1 + m_2, n_1 + n_2)$  are considered. Data are taken from  $r/a = 0.54$  and  $n_1 = n_2 = -5$  modes are shown. The local interaction among the resonant modes decreases for the case which retains non-resonant modes (a) in the later nonlinear phase, implying that the non-resonant modes mediate longer range interactions.

Figure 11 shows the radial profile of the average bicoherence near the location where the turbulence intensity peak forms ( $r/a \approx 0.6$ ). The result is obtained with a time average over the time interval  $t/\tau_s = 123 - 137$ , when the peak persists. The convective cells weaken the local interaction around  $\delta r = 0$  and strengthen the nonlocal interaction. The difference between the two cases is not apparent, due to the transient character of the simulation, which is dominated by profile relaxation. The broader fluctuation intensity profile in the presence of the convective cells in Fig. 10(b) is closely related to the increase (decrease) of nonlocal (local) interactions. In the same vein, the turbulence profile becomes broader on account of nonlocal spectral energy transfer, implying enhancement of turbulence spreading by convective cells. We confirm that the fluctuation intensity profile becomes broader with the increase of nonlocal interactions in the simulations with 160 M marker particles (see Fig. 12).

#### IV. EFFECTS ON REYNOLDS STRESS AND ZONAL FLOW

The difference in turbulence intensity profile caused by the suppression of the radially extended convective cells affects the Reynolds stress and zonal flow generation, because the time evolution of turbulence and zonal flow are obviously quite tightly coupled to one another. The turbulence-driven Reynolds stress and zonal flow increment are computed using Eq. (1). The radial profiles of Reynolds stress, zonal flow increment, and zonal flow are shown in Figs. 13 and 14 for the simulations with 40 M and 160 M marker particles, respectively. The profiles are averaged over

the period  $t = 135 - 155\tau_s$ . In the cases with suppressed non-resonant convective cells, the gradient of Reynolds stress increases at the middle radii ( $r/a \sim 0.5$ ) and a stronger zonal flow is driven. The stronger zonal flow increment can be understood as resulting from the peaked turbulence intensity profile from the relation in Eq. (1),  $\partial_t \langle V_{E \times B} \rangle \sim -\partial_r \langle \phi^2 \rangle$ . On the other hand, when we retain convective cells, the broad intensity profile caused by the enhanced turbulence spreading reduces the zonal flow increment, since  $|\partial_r \langle \phi^2 \rangle|$  is smaller. Figure 15 summarizes the effect of the convective cells on the self-generation of zonal flow.

From the equation of zonal flow generation in Eq. (1), we can also identify the correlation of fluctuating potential in  $k_r$  and  $k_\theta$  space as a key ingredient in Reynolds stress generation. Figure 16 shows the  $k_r - k_\theta$  spectra of fluctuating potential  $\phi^2(k_r, k_\theta)$  (a) without, and (b) with, non-resonant modes associated with convective cells. The data analyzed are taken at  $t = 135\tau_s$  when the difference between the two cases is most noticeable. The data are from  $r/a \approx 0.5$ , inside of the region where the turbulence intensity peak forms. The radial wave number spectra are obtained using the Fourier transform of the fluctuating potential within a radial interval of length  $L \sim 0.25a$ , so the resolution in  $k_r$  is  $\Delta k_r \approx 0.28\rho_{i0}^{-1}$ . When convective cells are suppressed, a clear asymmetry in the  $\phi^2(k_r, k_\theta)$  spectrum appears, as denoted by the black dashed line in Fig. 16(a). This asymmetry corresponds to radially outgoing propagation from the location of the turbulence intensity peak in Fig. 10(b). For the case with convective cells retained, an additional fluctuation structure with  $k_r k_\theta > 0$  arises (as denoted by the red, dashed line in Fig. 16(b)), with the result that the spectrum

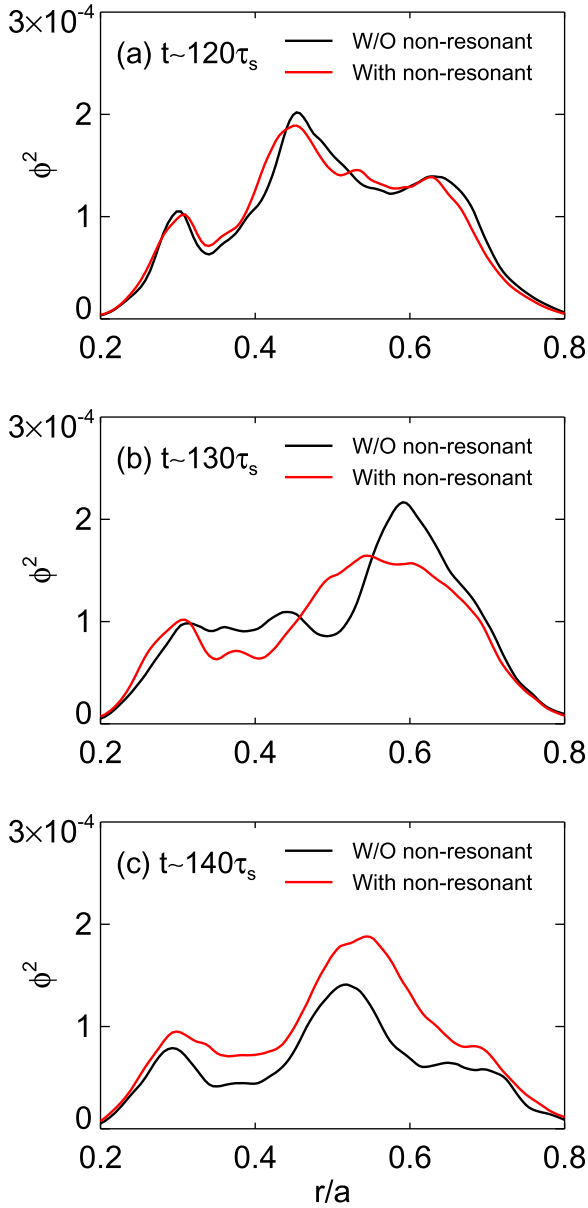


FIG. 10. Time evolution of the turbulence intensity profiles with (red), and without (black), non-resonant modes for simulations with 40 M markers.

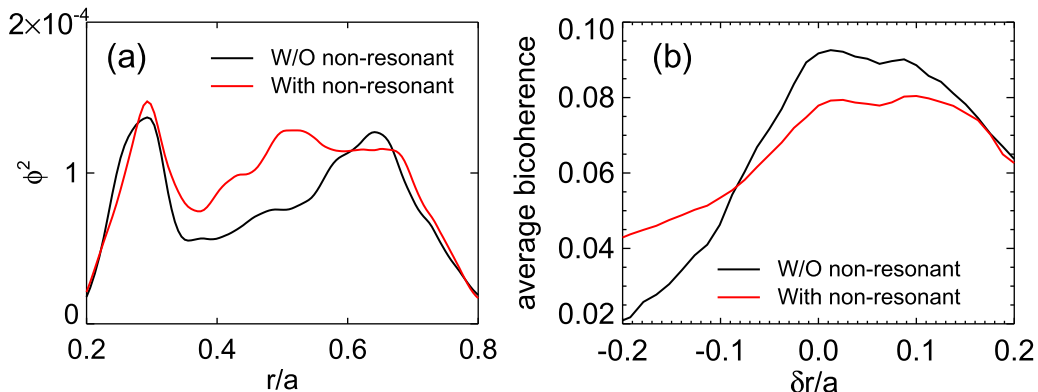


FIG. 12. Radial profiles of (a) turbulence intensity and (b) average bicoherence near the position  $r/a \approx 0.6$  averaged over the period  $t = 135 - 150\tau_s$  for simulations with 160 M markers.

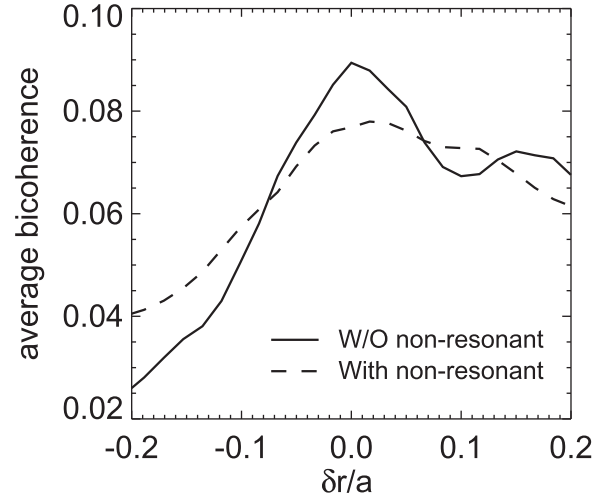


FIG. 11. Radial profile of average bicoherence with (broken), and without (solid), non-resonant modes near the position  $r/a \approx 0.6$  for simulations with 40 M markers.

becomes more symmetric. The additional fluctuation structure is associated with propagation opposite to the outgoing direction. This opposite direction propagation increases concomitantly with the decrease of the turbulence localization caused by the enhanced turbulence spreading. The more symmetric spectrum in the case with non-resonant modes is consistent with the decrease of the Reynolds stress in the middle radii in Fig. 13(a).

The  $\phi^2(k_r, k_\theta)$  spectrum also reflects the effect of zonal flow shearing on  $k_r$ . Recalling the eikonal theory for evolution of  $k_r$  with zonal flow shearing<sup>1</sup>

$$\frac{d}{dt}k_r = -\frac{\partial}{\partial r}[k_\theta V_{E \times B}(r)] \sim -k_\theta \frac{\partial V_{E \times B}}{\partial r},$$

we note that  $k_r$  increases with stronger zonal flow shearing. We confirm this by computing the average radial wave numbers from the spectra in Fig. 16, which is defined as

$$\langle k_r \rangle \equiv \frac{\sum_{k_r, k_\theta, \omega > 0} k_r \phi_{\mathbf{k}, \omega}^2}{\sum_{k_r, k_\theta, \omega > 0} \phi_{\mathbf{k}, \omega}^2}.$$

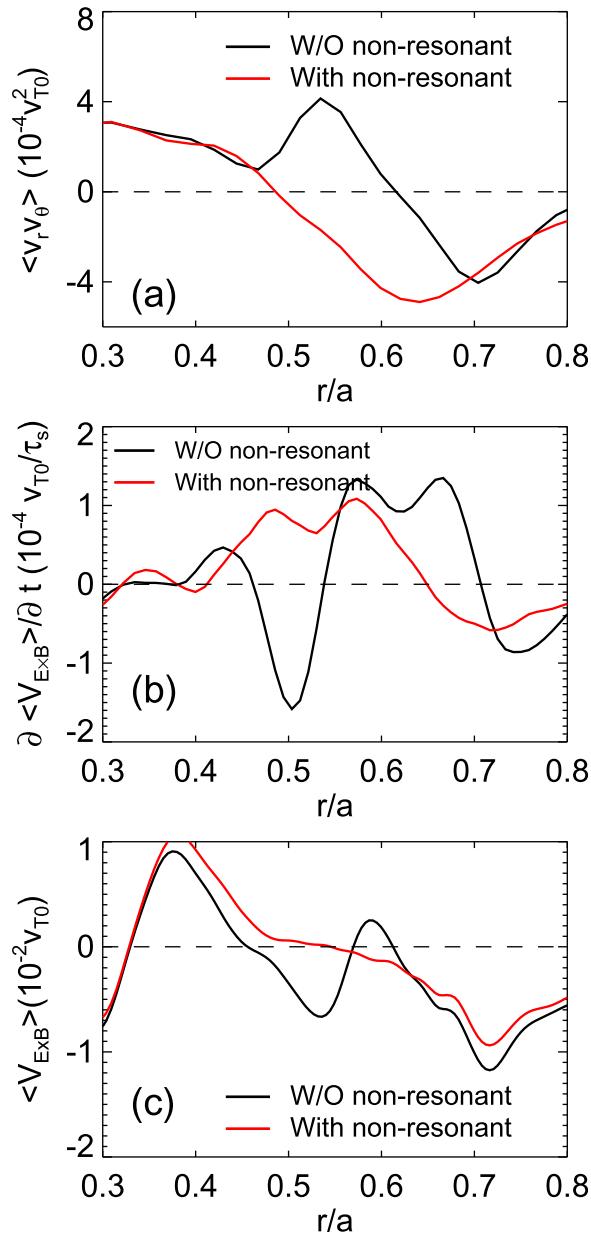


FIG. 13. Radial profiles of (a) Reynolds stress, (b) zonal flow increment, and (c) zonal flow averaged over the period  $t = 135 - 155\tau_s$  for simulations with 40 M markers.

The values are  $\langle k_r \rho_{i0} \rangle \approx 0.14$  for the case with stronger zonal flow shear and  $\langle k_r \rho_{i0} \rangle \approx -0.03$  for the case with reduced zonal flow shear.

Figure 17 shows time histories of (a) zonal flow increment, (b) zonal flow, and (c)  $E \times B$  shearing rate,  $\omega_{E \times B} \equiv \partial \langle V_{E \times B} \rangle / \partial r$ , around the central radii. A stronger drive of zonal flow at  $t = 130 - 140\tau_s$  appears when the radially extended convective cells are suppressed. The estimated zonal flow increment is consistent with the increase of the zonal flow and  $E \times B$  shearing rate.

## V. EFFECTS ON TURBULENCE AND TRANSPORT

When the radially extended convective cells are suppressed, turbulence is more effectively regulated due to the increase of zonal flow, as shown in Fig. 18(a)—the time his-

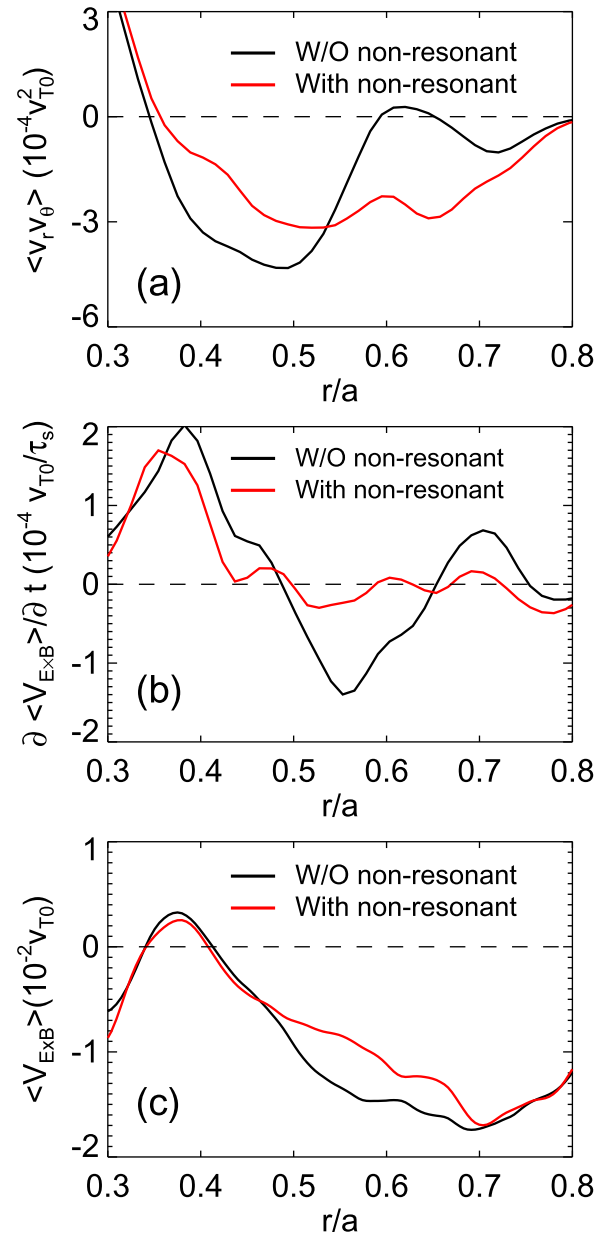


FIG. 14. Radial profiles of (a) Reynolds stress, (b) zonal flow increment, and (c) zonal flow averaged over the period  $t = 135 - 155\tau_s$  for simulations with 160 M markers.

tory of the total turbulence intensity integrated over the simulation volume, for the simulations with 40 M markers. (For the larger marker number simulations, turbulence level is higher in the case with retained convective cells.) Figure 18(b) shows the radial profile of the temperature gradient  $R_0/L_T$  during the times of enhanced turbulence regulation ( $t = 130 - 140\tau_s$ ). In the case with suppressed convective cells, the temperature perturbation is stronger. This is because the turbulence intensity peak around  $r/a \sim 0.6$  in Fig. 10(b) produces larger heat and momentum transport. We can interpret the production of larger Reynolds stress addressed in Sec. IV as the increase of momentum transport.

## VI. TOROIDAL ROTATION

In addition to zonal flows, toroidal rotation is an essential element in the dynamics of profiles and turbulence. From

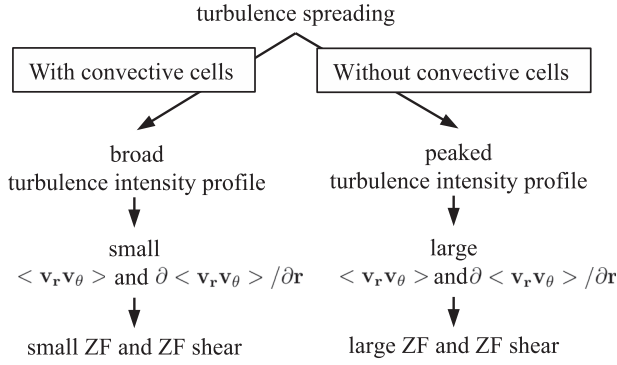


FIG. 15. Flow chart showing the effect of secondary convective cell on self-generation of zonal flow.

previous studies, we know that broken  $k_{\parallel}$ -symmetry in the fluctuation spectrum can generate intrinsic torque and drive toroidal plasma rotation.<sup>24,31</sup> In this section, we briefly report the effects of nonlinear interactions involving non-resonant modes (associated with the convective cells) on intrinsic toroidal rotation.

The radial profiles of toroidal rotation are shown in Fig. 19(a). The intrinsic rotation profiles are similar for the two cases during nonlinear phase ( $t \sim 155$ ) except the middle radius, where stronger zonal flow shear is driven without the non-resonant modes. Interestingly, a remarkable difference appears after the decay of turbulence by profile relaxation. Higher intrinsic rotation persists during the whole time interval in the case without non-resonant modes, while the rotation decreases in the case with non-resonant modes. Because this observation is limited to the late phase of the simulation when turbulence decays, the effect of the non-resonant modes on the toroidal rotation is modest.

The decrease in the flow is related to the decrease of parallel wave number asymmetry, i.e., decrease of mean parallel wave number  $\langle k_{\parallel} \rangle$ . The asymmetry in  $\langle k_{\parallel} \rangle$  can be evaluated from the potential fluctuation spectrum as

$$\langle k_{\parallel} \rangle = \frac{\sum_{m,n,\omega} \frac{m-nq}{qR_0} \phi_{m,n,\omega}^2}{\sum \phi_{m,n,\omega}^2}, \quad (6)$$

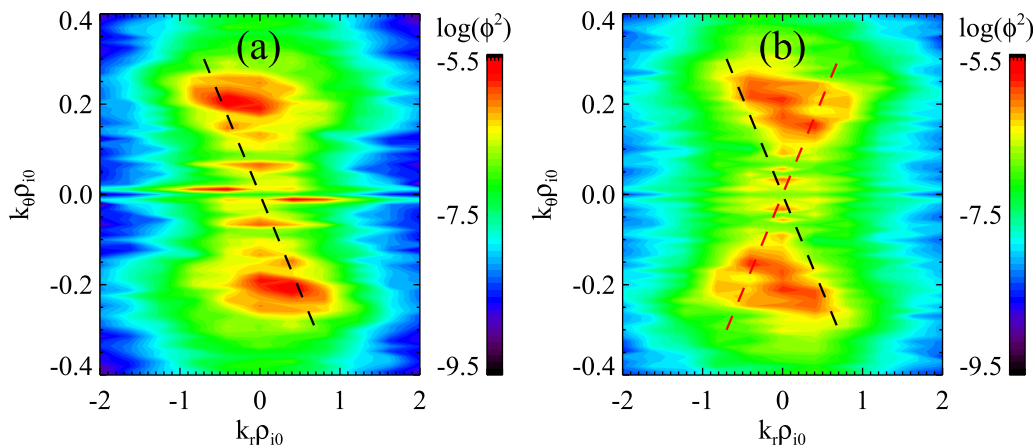


FIG. 16. Fluctuation spectra in  $k_r - k_\theta$ ,  $\phi^2(k_r, k_\theta)$ , in the cases (a) without, and (b) with, non-resonant modes around  $r/a \sim 0.5$  and at  $t = 135\tau_s$  for simulations with 40 M markers.

where  $\omega > 0$ . Compared in Fig. 19(b) are the  $\langle k_{\parallel} \rangle$  profiles before (black) and after the decay (red). Before the decay, the radial profiles of  $\langle k_{\parallel} \rangle$  in both cases are similar. After the decay at  $t \sim 225\tau_s$ , the profile of  $\langle k_{\parallel} \rangle$  significantly decreases in the outer radii ( $r/a > 0.6$ ) with non-resonant modes, while it hardly changes from its value of the time of saturation in the case without non-resonant modes. During the entire time of the simulation, the interactions involving the non-resonant modes continue to spread the modes with a finite  $k_{\parallel}$ , subjected to a constraints of total momentum conservation.

## VII. CONCLUSIONS AND DISCUSSION

We have presented the results of gyrokinetic simulation studies of the role of non-resonant modes in turbulence spreading and plasma zonal flow generation. Non-resonant modes may be thought of as radially extended convective cells with finite  $k_{\parallel}$ . Motivated by considerations of coupling between spatial spreading and spectral scattering of fluctuations via nonlinear interaction, we investigated the effects of non-resonant modes on the self-regulation dynamics of turbulence and plasma flows. The amplitude of the non-resonant modes grows continuously during the nonlinear phase. Non-resonant modes have broader radial extent and larger effective parallel wave number than do resonant modes. We identified and characterized the non-resonant modes as radially extended, secondary convective cells. Using comparisons between full simulations and studies with the cells switched off, we elucidated the relation between the role of the convective cells in turbulence spreading, the structure of the turbulence intensity profile, and the saturated turbulence level.

Results showed that the local interactions of resonant modes can be enhanced by suppressing the convective cells, which leads to a change in the spatial profile of turbulence intensity. The relation between the nonlinear interactions and turbulence spreading can be summarized as follows: (i) the interactions among the resonant modes, only, are more radially localized, and so yield a peaked turbulence intensity profile, (ii) the interactions involving the non-resonant modes, associated with radially extended convective cells,

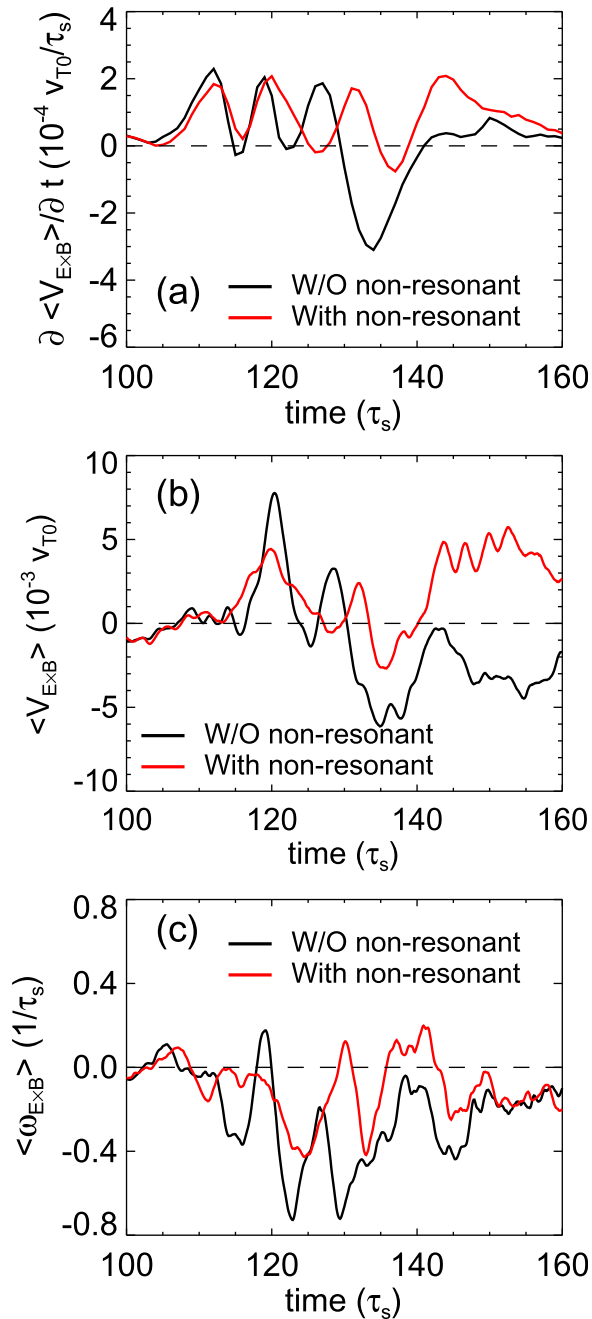


FIG. 17. Time histories of (a) zonal flow increment around  $r/a \approx 0.5$  and (b) zonal flow and (c) zonal flow shear averaged over the region  $r/a = 0.48$ – $0.51$  for simulations with 40 M markers.

are more distributed in radius, thus promote turbulence spreading and so cause the turbulence intensity profile to broaden. More peaked intensity profiles are more effective at driving zonal flows; other factors being equal and so should exhibit weaker turbulence and better confinement.

These studies unambiguously demonstrated that the turbulence spreading plays a significant role in the self-regulation dynamics. By suppressing the radially extended convective cells and thereby reducing turbulence spreading, we indeed showed that the resulting peaked spatial profile of turbulence intensity yielded a larger Reynolds stress. Thus, stronger  $E \times B$  shear flows were generated near the turbulence intensity gradient peak. As a consequence of the

increase of zonal flow, the turbulence level is significantly reduced.

Several aspects of these results merit discussion in the context of current issues in tokamak transport phenomenology. These are

1. Turbulence spreading is frequently invoked as a possible mechanism for nonlocal phenomena observed in tokamak experiments. Such nonlocality phenomena include the rapid core response to a cold pulse at the edge<sup>32,33</sup> and the increase of fluctuation levels at inner radii during the H-L back-transition.<sup>34</sup> Turbulence spreading can be experimentally identified by estimating the spatially dependent bicoherence of fluctuation data.<sup>35</sup> If turbulence spreading is a dominant process in these nonlocal phenomena, the bicoherence range may exceed the turbulence correlation length. Since we have shown that non-resonant modes play a role in turbulence spreading, it is likely that they are an element of the dynamics of nonlocality phenomena.
2. The dynamics of edge-core coupling in tokamaks is especially crucial to understanding the formation and extent of the H-mode pedestal. In particular, the extent and precise location of the domain connecting the core region to the edge-pedestal region—the so called “No Man’s Land”—is uncertain. And the turbulence level in the intermediate region deviates from most theoretical predictions based on local gradient-driven instabilities. Turbulence spreading likely plays a role in determining the turbulence level in the intermediate region by backwash or spillover from the strongly turbulent L-mode edge into the marginally stable core or by the breaking of core turbulence spreading on the “beach” of No Man’s Land.<sup>8–10</sup> Here, we argue that the efficiency of spreading is enhanced in regions where secondary convective cells are situated and so varies in radius. The dynamics and turbulence level of the intermediate region are influenced by profiles of the nonlinear scattering of turbulence intensity as well as linear growth. Thus, non-resonant modes are likely a significant element in the dynamics of No Man’s Land.
3. We note that most of transport models in use today are based on the local features of turbulence structure. The level of fluctuations is usually determined by mixing-length rules linking the linear growth rate and the dominant  $E \times B$  nonlinearity<sup>36</sup> or by a saturation rule determined by fits to nonlinear gyrokinetic turbulence simulations, which are local in both position and spectral space.<sup>37</sup> Discrepancies between transport models and experimental measurements still exist and may arise from the local approximations of turbulence properties. We believe that the present study demonstrates the importance of nonlocal coupling between spectral modes in turbulence and transport. The gap between transport models and experiment might be bridged by a nonlocal model for the effective mixing length scale and the saturation level of fluctuations, including the spatial flux of fluctuation energy driven by spectral interactions. To this end, proper treatment of non-resonant modes seems essential to accurately calculate the fluctuation envelope structure and zonal flow generation.

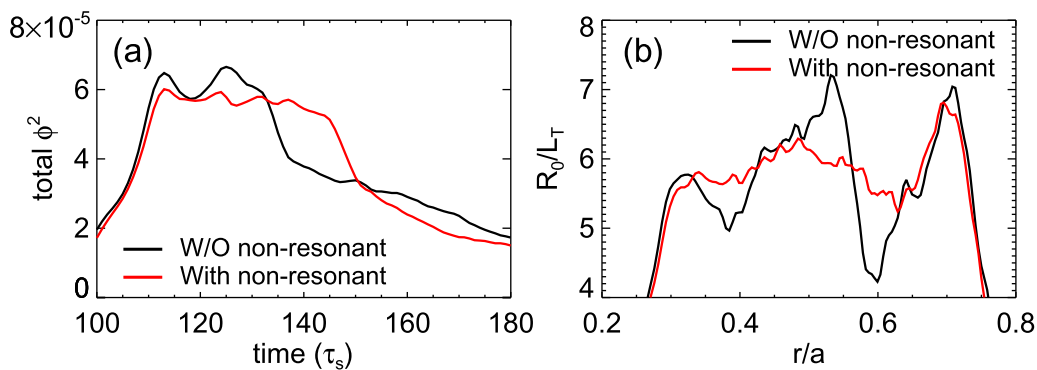


FIG. 18. (a) Time histories of the total turbulence intensity and (b) radial profiles of temperature gradient  $R_0/L_T$  averaged over the period  $t = 130 - 140\tau_s$  for simulations with 40 M markers.

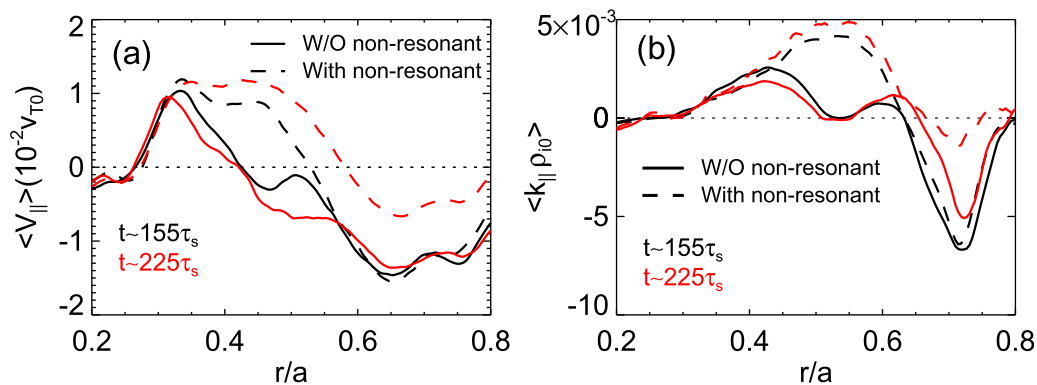


FIG. 19. Radial profiles of (a) the toroidal rotation and (b) parallel wave number asymmetry  $\langle k_{\parallel} \rangle$  in the cases with (broken), and without (solid), non-resonant modes immediately after ( $t \sim 155$ ) and long after the decay of turbulence ( $t \sim 225$ ) for simulations with 40 M markers.

To reliably reproduce and understand the formation of transport barriers using computer simulations, such simulations should reflect the experimental realities more faithfully and include such effects as external momentum sources that may assist the mitigation of ion temperature profile stiffness. In a related vein, the effects of plasma rotation and its shear on the nonlinear interactions and spatial spreading of turbulence will be an important subject for future works. Also, it will be interesting to study how relaxation of the assumptions inherent in this simulation, such as adiabatic electron response, will change the nature of nonlinear interactions involving non-resonant modes.

In future works, we will study roles of nonlinear interactions and turbulence spreading in turbulence self-organization and transport barrier formation using a global flux-driven gyrokinetic model, which can achieve the required steady state simulation. We will revisit the observations in the present study without the transient features and so obtain a clearer interpretation of the physics of non-resonant modes and their roles in the self-regulation dynamics of confined plasma turbulence and flows.

## ACKNOWLEDGMENTS

We wish to thank (in alphabetical order) J. Abiteboul, G. Dif-Pradalier, X. Garbet, V. Grandgirard, Ö. Gürçan, J. Y. Kim, S. Ku, Y. Sarazin, A. Strugarek, and the participants in the 2011 Festival de Theorie for interesting discussions. S.

Yi acknowledges the hospitality of C.E.A., Cadarache, during a visit where part of this work was performed. This work was supported by the World Class Institute (WCI) Program of the National Research Foundation of Korea (NRF) funded by the Ministry of Education, Science and Technology of Korea (MEST) (NRF Grant No. WCI 2009-001) and by CMTFO funded by the U. S. DOE Grant No. DE-FG02-04ER54738.

- <sup>1</sup>P. H. Diamond, S.-I. Itoh, K. Itoh, and T. S. Hahm, *Plasma Phys. Controlled Fusion* **47**, R35 (2005).
- <sup>2</sup>P. W. Terry, *Rev. Mod. Phys.* **72**, 109 (2000).
- <sup>3</sup>P. H. Diamond and Y.-B. Kim, *Phys. Fluids B* **3**, 1626 (1991).
- <sup>4</sup>P. H. Diamond, Y.-M. Liang, B. A. Carreras, and P. W. Terry, *Phys. Rev. Lett.* **72**, 2565 (1994).
- <sup>5</sup>X. Garbet, L. Laurent, A. Samain, and J. Chinardet, *Nucl. Fusion* **34**, 963 (1994).
- <sup>6</sup>T. S. Hahm, P. H. Diamond, Z. Lin, K. Itoh, and S.-I. Itoh, *Plasma Phys. Controlled Fusion* **46**, A323 (2004).
- <sup>7</sup>Z. Lin and T. S. Hahm, *Phys. Plasmas* **11**, 1099 (2004).
- <sup>8</sup>Ö. D. Gürçan, P. H. Diamond, T. S. Hahm, and Z. Lin, *Phys. Plasmas* **12**, 032303 (2005).
- <sup>9</sup>T. S. Hahm, P. H. Diamond, Z. Lin, G. Rewoldt, Ö. D. Gürçan, and S. Ethier, *Phys. Plasmas* **12**, 090903 (2005).
- <sup>10</sup>Ö. D. Gürçan, P. H. Diamond, and T. S. Hahm, *Phys. Rev. Lett.* **97**, 024502 (2006); *Phys. Plasmas* **13**, 052306 (2006).
- <sup>11</sup>X. Garbet, C. Bourdelle, G. T. Hoang, P. Maget, S. Benkadda, P. Beyer, C. Figarella, I. Vitsekhovitch, O. Agullo, and N. Bian, *Phys. Plasmas* **8**, 2793 (2001).
- <sup>12</sup>X. Garbet, Y. Sarazin, Ph. Ghendrih, S. Benkadda, P. Beyer, C. Figarella, and I. Vitsekhovitch, *Phys. Plasmas* **9**, 3893 (2002).
- <sup>13</sup>S. S. Kim, H. Jhang, P. H. Diamond, L. Terzolo, S. Yi, and T. S. Hahm, *Nucl. Fusion* **51**, 073021 (2011).

- <sup>14</sup>Y. Sarazin, A. Strugarek, G. Dif-Pradalier, J. Abiteboul, S. Allfrey, X. Garbet, Ph. Ghendrih, V. Grandgirard, and G. Latu, *J. Phys.: Conf. Ser.* **260**, 012017 (2010).
- <sup>15</sup>S. C. Cowley, M. Kulsrud, and R. Sudan, *Phys. Fluids B* **3**, 2767 (1991).
- <sup>16</sup>P. Beyer, S. Benkadda, X. Garbet, and P. H. Diamond, *Phys. Rev. Lett.* **85**, 4892 (2000).
- <sup>17</sup>Y. Sarazin, V. Grandgirard, J. Abiteboul, S. Allfrey, X. Garbet, Ph. Ghendrih, G. Latu, A. Strugarek, and G. Dif-Pradalier, *Nucl. Fusion* **50**, 054004 (2010).
- <sup>18</sup>J. F. Drake, P. N. Guzdar, and A. B. Hassam, *Phys. Rev. Lett.* **61**, 2205 (1988).
- <sup>19</sup>P. H. Diamond and T. S. Hahm, *Phys. Plasmas* **2**, 3640 (1995).
- <sup>20</sup>S. Champeaux and P. H. Diamond, *Phys. Lett. A* **288**, 214 (2001).
- <sup>21</sup>P. H. Diamond, S. Champeaux, M. Malkov, A. Das, I. Gruzinov, M. N. Rosenbluth, C. Holland, B. Wecht, A. I. Smolyakov, F. L. Hinton, Z. Lin, and T. S. Hahm, *Nucl. Fusion* **41**, 1067 (2001).
- <sup>22</sup>H. Okuda and M. J. Dowson, *Phys. Fluids* **16**, 408 (1973).
- <sup>23</sup>R. Z. Sagdeev, V. D. Shapiro, and V. I. Shevchenko, *Sov. J. Plasma Phys.* **4**, 306 (1978).
- <sup>24</sup>J. M. Kwon, S. Yi, T. Rhee, P. H. Diamond, K. Miki, T. S. Hahm, J. Y. Kim, Ö. D. Gürcan, and C. McDevitt, *Nucl. Fusion* **52**, 013004 (2012).
- <sup>25</sup>T. S. Hahm, *Phys. Fluids* **31**, 2670 (1988).
- <sup>26</sup>M. Fivaz, S. Brunner, G. de Ridder, O. Sauter, T. M. Tran, J. Vaclavik, L. Villard, and K. Appert, *Comput. Phys. Commun.* **111**, 27 (1998).
- <sup>27</sup>Y. Idomura, S. Tokuda, and Y. Kishimoto, *Nucl. Fusion* **43**, 234 (2003).
- <sup>28</sup>S. Jolliet, A. Bottino, P. Angelino, R. Hatzky, T. M. Trana, B. F. Mcmillan, O. Sauter, K. Appert, Y. Idomura, and L. Villard, *Comput. Phys. Commun.* **177**, 409 (2007).
- <sup>29</sup>Y. C. Kim, J. M. Beall, E. J. Powers, and R. W. Miksad, *Phys. Fluids* **23**, 258 (1980).
- <sup>30</sup>K. Itoh, Y. Nagashima, S.-I. Itoh, P. H. Diamond, A. Fujisawa, M. Yagi, and A. Fukuyama, *Phys. Plasmas* **12**, 102301 (2005).
- <sup>31</sup>P. H. Diamond, C. J. McDevitt, Ö. D. Gürcan, T. S. Hahm, and V. Naulin, *Phys. Plasmas* **15**, 012303 (2008).
- <sup>32</sup>K. W. Gentle, R. V. Bravenec, G. Cima, G. A. Hallock, P. E. Phillips, D. W. Ross, W. L. Rowan, A. J. Wootton, T. P. Crowley, A. Ouroua, P. M. Schoch, and C. Watts, *Phys. Plasmas* **4**, 3599 (1997).
- <sup>33</sup>S. Inagaki, K. Ida, N. Tamura, T. Shimozuma, S. Kubo, Y. Nagayama, K. Kawahata, S. Sudo, K. Ohkubo, and LHD Experimental Group, *Plasma Phys. Controlled Fusion* **46**, A71 (2004).
- <sup>34</sup>T. Estrada, C. Hidalgo, and T. Happel, *Nucl. Fusion* **51**, 032001 (2011).
- <sup>35</sup>Ö. D. Gürcan, private communication (2011).
- <sup>36</sup>J. Weiland, A. B. Jarmén, and H. Nordman, *Nucl. Fusion* **29**, 1810 (1989).
- <sup>37</sup>G. M. Staebler, J. E. Kinsey, and R. E. Waltz, *Phys. Plasmas* **14**, 055909 (2007).